Micro and macro mechanical characterization of artificial cemented granular materials

Abbas Farhat, Li-Hua Luu, Alexis Doghmane, Pablo Cuéllar, Nadia
Benahmed, Torsten Wichtmann, Pierre Philippe

HAL Id: hal-04582962

https://hal.inrae.fr/hal-04582962

Submitted on 22 May 2024

Micro and macro mechanical characterization of artificial cemented granular materials

Abbas FARHAT[1,3*], Li-Hua LUU[1†], Alexis DOGHMANE[1†], Pablo CUÉLLAR[2†], Nadia BENAHMED[1†], Torsten WICHTMANN[3†], Pierre PHILIPPE[1†]

[1*]RECOVER, INRAE-Aix Marseille univ., 3275 Route Cézanne, Aix en Provence, 13100, France.
[2]Division 7.2 "Buildings and Structures", BAM Bundesanstalt für Materialforschung und-prüfung, Unter den Eichen 87, Berlin, 12205, Germany.
[3]Institute of Soil Mechanics and Foundation Engineering, Ruhr University Bochum, Universitätsstraße 150, Bochum, 44801 , Germany.

*Corresponding author(s). E-mail(s): abbas.farhat@inrae.fr;
Contributing authors: li-hua.luu@inrae.fr; alexis.doghmane@inrae.fr;
pablo.cuellar@bam.de; nadia.benahmed@inrae.fr;
torsten.wichtmann@rub.de; pierre.philippe@inrae.fr;
[†]These authors contributed equally to this work.

Abstract

The focus of this study is the experimental characterization of cemented granular materials, with the aim of identifying the microscopic properties of the solid bonds and describing the extension to macroscopic mechanical strength of cemented samples. We chose to use artificially bonded granular materials, made of glass beads connected by solid paraffin bridges. The results of several sets of laboratory tests at different scales are presented and discussed. Micromechanical tests investigate the yield strength of single solid bonds between particles under traction, shearing, bending and torsion loading, as a function of variations in particle size, surface texture and binder content. Macro-scale tensile tests on cemented samples explore then the scale transition, including influence of confining walls through homothetic variations of the sample size. Despite the large statistical dispersion of the results, it was possible to derive and validate experimentally an analytical expression for micro tensile yield force as a function of the binder content, coordination number and grain diameter. In view of the data, an adhesive

bond strength at the contact between bead and solid bond is deduced with very good accuracy and it is even reasonable to assume that the other threshold values (shear force, bending and torsion moments) are simply proportional to the tensile yield, thus providing a comprehensive 3D model of cemented bond. However, the considerable dispersion of the data at the sample scale prevents validation of the extended model for macroscopic yield stress. A final discussion examines the various factors that may explain intrinsic variability. By comparison with other more realistic systems studied in the literature in the context of bio-cementation, our artificial material nevertheless appears suitable for representing a cemented granular material. Being easy to implement, it could thus enable the calibration of discrete cohesion models for simulation of practical applications.

1 Introduction

Somewhere between hard soils and soft rocks exists a somehow marginal class of geomaterials consisting of cemented soils. These soils are characterised by the presence of a binder that connects their constituent particles and confer them specific mechanical properties such as enhanced tensile strength [1, 2]. Despite this reinforcement by cementation, the soil's macroscopic mechanical behavior may remain largely non-elastic, whereby brittle ruptures of single intergranular bonds may lead to large fractures at the macroscopic scale. Given the ubiquitous presence of cemented granular materials in the environment as well as in our civil constructions (e.g. hydraulic earthworks), it appears essential to fully understand this type of mechanical behaviour.

Many geological landforms all over the world consist indeed of several varieties of cemented soils such as sandstones, breccias, carbonate sands, or coarse-grained sediments [3–5]. The high shear strength of these geomaterials often creates dramatic landscapes characterised by cliffs with very steep slopes, shaped by sudden and consecutive collapse events [4]. Sandstone is also abundant in the deep seabed, which has motivated a growing interest from the offshore community seeking to operate at greater depths [6]. Such natural cementation has mainly an inorganic origin from precipitation and deposition of mineral compounds such as carbonates, commonly carried by underground flows [7, 8]. Hydrate-bearing sediments are another example of natural cementation [9, 10]. There are alternative cementing agents of biogenic origin, induced by biological activity (roots, microbes, bacteria, fungi) [1, 8]. Natural cementation is often accompanied by a substantial variability in strength observed on a large but also on a small scale [3].

Particles binding is also obtained from artificial cementation in several construction materials (mortar, asphalt) [5, 11] and commonly implemented on site for soil improvement [12]. Binding agents are typically cement, lime, bitumen, or polymeric organic stabiliser [12, 13] but, due to energy cost and greenhouse gas emission [14], alternative techniques are emerging, such as industrial waste residue-based binding [15] or microbially induced cementation [16]. These soil treatments can provide

2

increased shear strength, prevent scouring (for instance around a pipeline [17]) or inhibit sediment transport (particularly critical for polluting or radioactive particles). Many other industries besides civil engineering (e.g. mineral, agricultural, food, chemical, pharmaceutical) produce and handle bonded particulate materials, usually in the form of agglomerates or granules whose attrition and breakage properties have to be assessed properly [18–20]. The range of cemented materials is anyway quite wide and other examples may also include sintered ceramics, snow, or certain grains such as wheat [5, 18].

The type of cemented soil of interest in the present study involves coarse soil particles bonded by solid bridges at grain contacts. In the literature, the vast majority of the experimental investigations focusing on this type of material have been carried out with artificially cemented models. This is partly due to the inherent difficulties for the extraction of intact cemented materials on site [3] while, on the other hand, the use of artificial materials also allows a wide and controlled exploration of their physical and mechanical properties (e.g. the mechanical strengthening provided by cementation). The preparation of such artificial cemented materials requires the addition of a binding matrix to the base granular material and their careful mixture until reaching a homogeneous distribution of the binder. In this respect, most studies employ a workable matrix easy to blend and which often hardens after mixing, as cement, clay, hydrated lime, polymeric solution, epoxy resin, etc... An alternative is to directly induce the precipitation of a crystallised solid, typically calcite of microbial origin [2, 16, 21, 22], within the granular sample. The final spatial distribution of the matrix in the material can then differ, ranging from a quasi-uniform coating of the surface of the grains to a very localised distribution of the cementing binder at the contacts [1, 5, 13, 21, 23]. Note that we are only interested here in the case where solid bridges exist between the grains, thus discarding the reversible contact adhesion resulting from uniform coating [24] or chemical silanization [25] of the grains, which in fact reproduces a cohesive granular soil and not a cemented one.

To assess the behaviour of such artificial cemented soils at sample scale, a first essential step is the microscopic characterisation of the mechanical strength of a cementing bridge between two grains. From an experimental point of view, some studies have been carried out to measure the yield strength of an individual bridge in tension, shear and, more seldom, in bending and torsion [10, 22, 26–31]. In the case where the cemented contacts are created from a prior coating of the grains, the subsequent failure of a bridge generally takes places within the solid binder. On the contrary, for the case of an isolated solid bridge, which is the focus of the present study, several modes of failure are possible [22, 32]: cohesive (i.e. internal failure within the binder), adhesive (i.e. debonding failure at the interface between the binder and the grain), or mixed (i.e. combination of the two previous modes). A progressive bond damage can also be observed in some cases [5]. Together with the elastic properties of the bond, a critical parameter is its adherence, or adhesive strength, to the grain surface [18], which depends on the microscopic interaction between the molecules of the two solid bodies in contact. This adhesive strength is to be compared to the cohesive strength, or ultimate tensile yield stress, which is an intrinsic property of a material. On the modelling side, several micro-mechanical contact laws exist for bonded grains,

including yield conditions of bond rupture (in stress, force or energy) derived from adhesion theory for elastic solids [33, 34] or calibrated from experimental results in 2D or 3D [27, 29, 35], with the convenient possibility of direct implementation in numerical calculations based on the Discrete Element Method approach [36–42] to model the soil's behaviour at a representative scale. From an analytical point of view, this transition from the microscopic level to the macroscopic behaviour of a bonded granular material is done with the help of homogenisation laws, developed in the continuity of Rumpf's original work [13, 43–45].

In the present study, we employed a simplified model of cemented granular soil, which will be presented in detail in Section 2, as well as the experimental set-ups developed and implemented to generate: (i) sample-scale tensile tests; (ii) grains scale tests in tension, shear, bending, and torsion, including a version of the device specifically adapted to in operando X-ray scans. The results obtained will be described in Section 3, from the macro down to the microscopic scale, the latter requiring a large number of measurements due to the high statistical dispersion. Then, Section 4 explores the suitability of some scaling trends to gather all the experimental data based on theoretical considerations, which is shown to remain a challenging task due to the huge dispersion of results, particularly at the macro level. The possible origins and relevance of such dispersion at the different scales are then discussed, as well as the positioning of our artificial material in relation to the current literature. A final summary is provided in Section 5.

2 Experimental devices

2.1 Materials & sample preparation

In this study we have chosen to work with artificial systems consisting of monosize millimetric glass beads bonded together by solid paraffin bridges. The corresponding type of cementation is that of solid bonds at particles contact with no observable coating at the beads surface, see the direct visualizations below. The relevance of this somehow unrealistic system in the context of cemented soils will be discussed further in Section 4.3, in the light of the results obtained and by comparison with the few experimental data available in [22, 30, 31].

The beads were supplied by Sigmund-Lindner GmbH and are made either of silicate or borosilicate glass, with density $\rho_{gs} = 2650$ kg/m^3 and $\rho_{gb} = 2230$ kg/m^3, respectively. We used separate particle lots, each with a narrow particle size distribution around a mean value. The diameters considered are $d = 0.60 \pm 0.13$ mm, $d = 1.40 \pm 0.15$ mm, $d = 3.0 \pm 0.3$ mm, and $d = 4.0 \pm 0.3$ mm for the silicate glass beads, and $d = 5.0 \pm 0.2$ mm and $d = 7.0 \pm 0.3$ mm for the borosilicate ones, respectively. The beads have two different surface finishes: a rough texture referred to as Matt (M) by the manufacturer and a smooth surface referred to as Polished (P). The typical Young modulus is $E_{gs} \sim 70$ GPa and $E_{gb} \sim 65$ GPa for the silicate and borosilicate glass, respectively.

The solid bonds are made from a commercial paraffin (supplied by Chimie-Plus Laboratoires) whose (solid) density was measured about 880 kg/m^3 and whose melting temperature is estimated around 50 °C. The volume reduction of liquid paraffin after

cooling (i.e. solidification) is small (see Figure 1) and was measured to be about 10 % (giving a liquid density around 800 kg/m^3). Note that this very low volume shrinkage is an improvement over the similar system developed previously in our group using polyurethane resin, whose high volume reduction on drying was suspected to weaken the solid bridge by generating pre-stresses and micro-fractures [46]. The Young's modulus of the solid paraffin was not determined in this study. However, literature values for different types of paraffin wax suggest that the Young's modulus is in the range of 100 MPa[47] to 200 MPa [48]. These values are much smaller than the moduli of the glass beads, indicating that only the bond is susceptible to deformation during a tensile test, while the glass beads remain rigid.
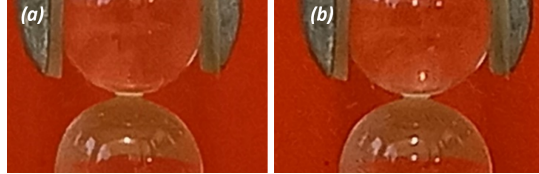
Fig. 1 Hardening of a paraffin bond from (a) liquid to (b) solid. Note that the reduction in volume of the bond is hardly observable by eye and that the shape of the bond remains pendular. The glass beads diameter is 4 mm.

A cemented sample is prepared using glass beads as granular material and liquid paraffin as binder. The corresponding paraffin content in mass is denoted $X_p = m_p/m_g$ (where mg and mp denote respectively the total mass of the glass beads and paraffin) and ranges here from 0.2 % to 1 %, while the volume fraction in paraffin directly reads $\xi_p = X_p\ \rho_g/\rho_p$ with ρ_g the glass density (either ρ_{gs} or ρ_{gb}). The mixture is heated with an electric stove set at 90 °C in order to reach a temperature in the medium high enough for the paraffin to be completely melted. At the same time, the sample is mixed carefully and continuously in order to uniformly distribute the liquid paraffin. The hot mixture is delicately poured through a funnel (keeping a small fall height) into a macroscopic scale mold made either of small, medium or large cones (see Figure 2). Finally, the sample is left at least for 7 hours to completely cool down at ambient temperature until complete hardening of all paraffin bonds. If the paraffin content is low enough, typically $X_p < 1\%$, only bonds with pendular shape are observed similar to Fig. 1. Beyond this range, there will be an increasing fraction of funicular bridges involving more than two particles. This observation is fully consistent with what is known about the distribution of water capillary bridges in a saturated soil [49]. In order to remain in the pendular regime, the paraffin mass content will not exceed 1% in the following experiments. Note that when $X_p = 0.2$ %, the bonds are so weak for the smallest particle size tested, namely $d = 1.4$ mm, that the extraction of pairs of beads becomes a very challenging task.

2.2 Macroscopic tensile tests

The present device is an improvement of an earlier version previously used to measure the tensile strength of a cemented granular sample [46]. It is based on the force required

to separate two inverted cones containing the material under test, the bottom cone being fixed while the top one is mobile. Practically, the two open conical containers are prior brought into contact in a horizontal plane at their minimum section. The granular sample, prepared as described previously in Section 2.1, is then poured from the top with the paraffin bridges being still in the liquid state. An average solid volume fraction of the order of 0.6 was consistently obtained in the samples from bead mass and mold volume. After solidification of the paraffin, an incremental tensile force is gradually applied to the upper cone via an interposed spring, as shown in Figure 3.

Fig. 2 The three homothetic cone sizes of the macro-scale tensile devices. The dimensions are in mm.

Specifically, the spring is connected at its base to the upper cone and at its top to a force sensor (via a hook), which is attached to the speed-controlled vertical translation module. The objective is to obtain a progressive increase of the applied force while concentrating the totality of the deformation within the spring. Homothetic cone devices in three different sizes (see Fig. 2) were used for the tests to assess the influence of the rupture area on the measured sample strength.

The applied uplift rate of the loading frame was set to either 0.3 mm/min for expected strong tensile forces (mainly with the large cones) or 0.1 mm/min for the other force values (usually for small and medium cones). The force supplied by the sensor is recorded over time (or equivalently displacement). Note that this force is not directly the tensile one since we need to subtract the global weight of the upper cone after separation, which can be done only at the end of the test. A typical test example is shown in the inset of Fig. 3. After a short initial regime where the extension of the spring is not linear, we quickly observe a regular increase of the tensile force measured by the sensor, until the sample ultimately breaks. After stabilization, we also measure the residual force, i.e. the weight of the upper part that remains suspended. The difference between maximum and residual forces provides the critical tension force F_T.

The geometry of the device concentrates the stresses at the contact area between the two cones to generate the rupture in this plane. The critical tensile stress σ_T is
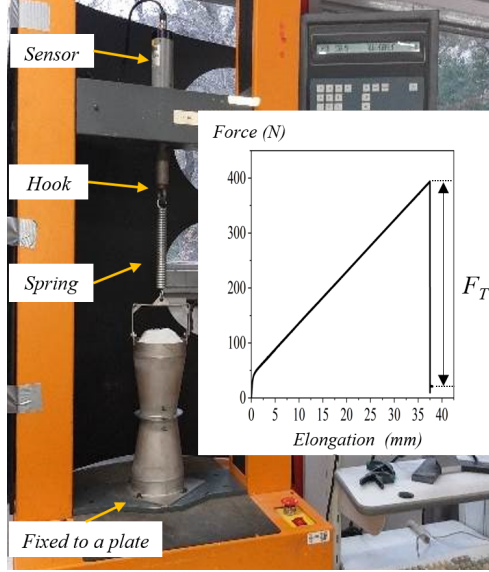
Fig. 3 Picture of the macroscopic traction device. Inset: A typical measurement of the force increasing with elongation until final rupture.

thus equal to the ratio of the force to the circular section of the failure zone:

$$\sigma_T = \frac{F_T}{A_D} \tag{1}$$

where $A_D = \frac{\pi}{4}D^2$ is the area at the neck cross section for the macroscopic device of diameter D.

Note however that, from what we observed during the tests and as will be discussed later, it appears that the shape of the rupture surface can substantially deviate from a simple plane, especially for large grains, presumably due to finite size effect.

All the 58 tests implemented at the macroscopic scale (with the 3 cone sizes) are reported below in Table 1.

2.3 Microscopic tests

Identifying the mechanical behavior at the scale of a solid bond between grains is essential and has led to the development of several micro-scale test devices in the literature, mainly in tension but also in shear, bending, and torsion [10, 22, 26–29]. This is also what we have done here by retaining a device based on the same principle as the previous macroscopic one as detailed below.

2.3.1 Tensile setup

A test was developed at the scale of a single adhesive bond connecting a pair of beads, in order to measure the tension force required to detach the beads. In principle, this

Particle diameter (mm)	Surface roughness	Paraffin mass content (%)	Particle type
0.6 ±0.13	P	0.2	S
	P	0.5	
	P	0.7	
1.40 ± 0.15	P	0.2	S
	P	0.5	
	P	0.7	
3.0 ± 0.3	P	0.2	S
	P, M	0.5	
	P	0.7	
	P	1.0	
4.0 ± 0.3	P	0.2	S
	P	0.5	
	P	0.7	
	P	1.0	
5.0 ± 0.2	P, M	0.5	BS
7.0 ± 0.3	P, M	0.5	S, BS

Table 1 Parameters for the macro-tensile characterization tests. P: polished; M: matt; S: silicate glass; BS: borosilicate glass.

system is comparable to the macroscopic one described in the previous section, with a similar spring insertion to gradually increase the force without deformation of the solid bridge. Here, however, as the forces considered are very small (mainly less than 1 N), a very low stiffness is required in order to concentrate all the deformation. To achieve this, the spring is handmade from metal wire, with more or fewer loops. Two different springs were used, a very soft one with an effective stiffness of 0.027 N/mm for forces much less than 1 N (used up to 4 mm particle size), and a soft one with an effective stiffness of 0.31 N/mm for forces around or slightly higher than 1 N (used for 5 mm and 7 mm particle sizes).

To keep exactly the same configuration as at the material scale, the two bonded beads tested are collected from the macroscopic cones after a tensile test, carefully extracted in the direct vicinity of the breakage surface through the macroscopic samples to be tested. Note that when $X_p = 0.2$ %, the bonds are so weak for the smallest particle size tested, namely $d = 1.4$ mm, that the extraction of pairs of beads becomes a very challenging task. Then, the tensioning system is set up vertically, with the lower bead glued to the surface of a wooden base using a drop of super glue (Loctite brand Super Glue-3), while the upper bead is held between the jaws of an inverted bulldog tweezers. The bulldog tweezers are connected to an inverted balance via the soft spring. A sketch of the set-up is shown in Figure 4a.

Once the bonded beads are correctly positioned, the tensile test can begin by recording the changes in mass on the balance while gradually lowering the lower bench by means of a settling table. As illustrated in Figure 5, the force progressively increases with time as the spring gets pulled apart, until bond failure. After debonding, a residual force is measured, corresponding to the remaining weight (spring, tweezers, upper bead, and any remaining solid bridge). Finally, the yield tensile force F_t is given by the force decrease at rupture.
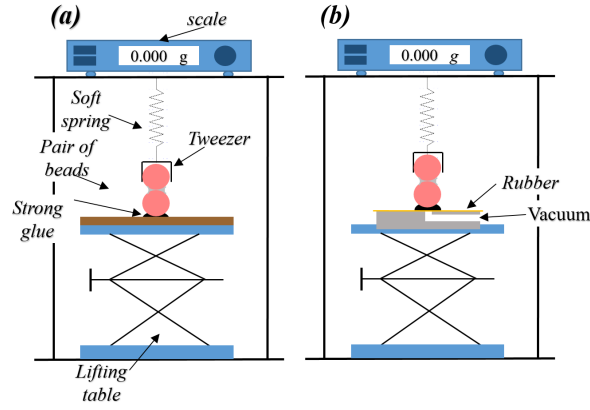
Fig. 4 Microscopic tensile scale devices, (a) using superglue method and (b) using suction method
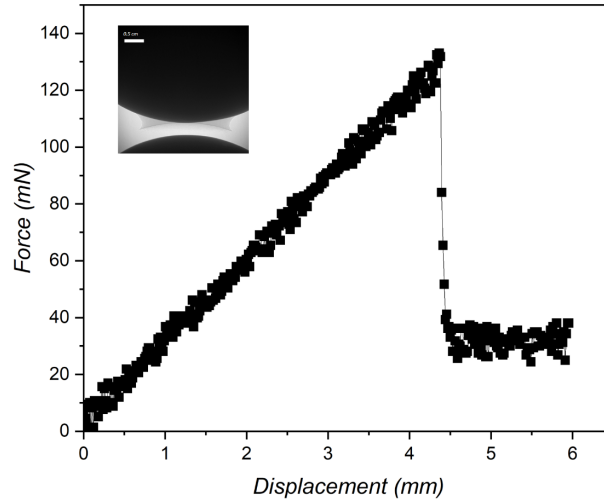
Fig. 5 Recorded tensile force measurements for 7mm matt glass beads with a paraffin mass content $X_p = 0.5$ % as a function of displacement of the settling table. Inset: 2D visualization of the paraffin bond after the adhesive rupture.

The time required to perform a single tensile test using this device has been a significant concern, with more than half an hour needed for the glue to dry completely in order to reach tensile forces higher than 0.3 N. Otherwise, detachment takes place at the glued contact. To address this issue, we improved the set-up by incorporating a thin rubber layer and a vacuum system beneath the lower bead as illustrated in Fig. 4b. The procedure involves first aligning vertically one of the beads using tweezers before gluing the lower bead to the rubber, which then undergoes shrinkage and adheres to the bead. Finally, the assembly is placed on the vacuum pit. As a result of these modifications, the average test time has been reduced to no more than 15 minutes, while allowing for higher tensile forces of up to 2 N or more, depending on the suction and bulldog tweezers used. Both versions, with and without the rubber and vacuum

system, have been utilized for studying tensile forces at the microscopic scale. It is worth noting that there is no fluctuation of the recorded data, and the descent speed of the bottom bead via the lifting table is manually controlled. A motorized version will be presented later.

As listed below in Table 2, we have performed about 350 micro-tensile tests in total, by varying the particle diameter and the paraffin mass content, with repetitions of 10 to 30 measurements for each test.

Particle diameter (mm)	Surface roughness	Paraffin mass content (%)	Particle type
1.40 ± 0.15	P	0.2	S
	P	0.5	S
	P	0.7	S
3.0 ± 0.3	P	0.2	S
	P, M	0.5	S
	P	0.7	S
	P	1.0	S
4.0 ± 0.3	P	0.2	S
	P	0.5	S
	P	0.7	S
	P	1.0	S
5.0 ± 0.2	M	0.5	BS
	M	1.0	BS
7.0 ± 0.3	M	0.4	BS
	P, M	0.5	S, BS

Table 2 Parameters for the micro-tensile characterization tests. P: polished; M: matt; S: silicate glass; BS: borosilicate glass.

2.3.2 Adaptation for shear, bending, and torsion

The micromechanical test setup was then modified to investigate the respective yielding limits under shear, torsion and rolling loads, as depicted in Figure 6. Compression was not considered among the mechanical loading configurations likely to cause bond failure. Indeed, since glass beads are always in direct contact and are far much stiffer than solid paraffin, compression does not stress the bond, but only the glass-glass contact between the two beads. It should be noted, however, that a recent study has investigated this configuration, but in the case where the beads do not touch each other [50].

The shear configuration is close to the tensile one but the pair of bonded beads is now placed horizontally and perpendicular to the tweezers, causing shear at the interfaces between paraffin and particle. In the case of torsion and bending load types, the moment is induced by an additional wood rod glued to the mobile bead and connected to the tweezers. It is important to note that a small normal force is applied as well, but it is weak and can be neglected. Similarly a small induced moment is applied to the bond in the shear configuration.

While, as expected and illustrated in Fig. 5, a linear increase in force with spring elongation over time is systematically observed for tension and shear tests, this is not
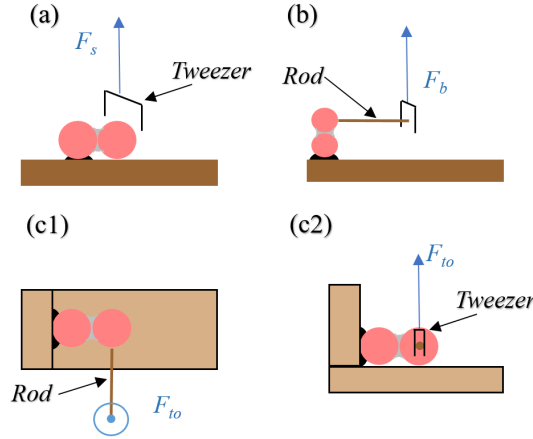
Fig. 6 Sketches of the different microscopic configurations for (a) shear, (b) bending, and (c) torsion in (c1) top view and (c2) side view.

always the case for torsion and bending configurations where unexpected behaviors are often observed, namely drops in force or loss of linearity as will be presented later in the forthcoming Section 3.3. After ruling out any possible slippage at the tweezers fixation or damage to the stick used as a lever arm, we upgraded the experimental set-up in order to elucidate the movements of particles responsible for this unexpected bending or torsion force evolution from image processing. To this aim, marker flags were placed on the two beads and the rod (see Figure 7 for the bending case) while the elongation of the spring and flag displacements were then recorded simultaneously using separate high-resolution cameras, namely Optronis Cyclone-25-150-M camera ($2048{\times}5120$ pixels^2) and XIMEA XiQ camera ($2048{\times}2048$ pixels^2), respectively.
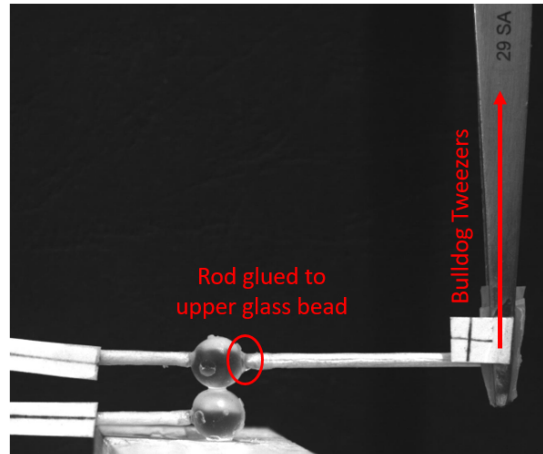
Fig. 7 Fixation of the rod to the upper glass bead and positions of the flags.

11

2.3.3 Development of a more compact microscopic device for micro-CT scans

To investigate the geometrical properties of a solid bridge between two particles and its different modes of rupture in greater detail, we conducted a few complementary micro-tomographic visualizations at the MATRIX[1] facility of the CEREGE laboratory in Aix-en-Provence. The micro-tensile setup was therefore adapted so that it could fit inside the tomography chamber for in operando use, i.e. obtaining tomography scans during the course of a mechanical test. One of the main objectives here is to investigate whether small-scale damage can be observed within a paraffin bridge before it fails.

The tomography device used for acquisition includes a X-ray source (target W, acceleration voltage 40 kV, power 10 W) and allows to record either fast 2D radiography images or scans for full 3D-reconstruction. The sample is positioned on a circular turntable with a clamping ring that can translate along the x-, y-, and z-axes, and also rotate around z-axis. In this experiment, a thin metallic hollow tube was fixed in the clamping ring and, for each tested pairs, one of the beads is glued on top of the tube. It is worth noting that the turntable is only moved or rotated after rupture to avoid applying additional load or damaging the bond. The exposure time for the radiography images was one second with a field view of $1024{\times}1024$ pixels^2. The loading setup included again the tweezers with the 0.31 N/mm stiffness spring, while the loads were measured with a compact force sensor mounted on a motor-driven translation plate. During the test, the force variation resulting from the motorized lifting movement of the upper plate at a constant speed is recorded.

3 Experimental results

In this section, we present all the results obtained from the experimental set-ups presented above, firstly at the scale of the cemented soil sample and then at that of the solid bonds between grains

3.1 At macro-scale

From the approximately 50 tests carried out on the macroscopic device, the critical tensile stress σ_T can be derived from the measured maximum tensile force F_T on the basis of Eq. 1 and plotted as a function of the paraffin content, quantified here by its volume fraction ξ_p. Figure 8 shows all measured values of (σ_T) as a function of ξ_p, including variations of both the bead diameter, from 0.6 mm to 7 mm, and on the size of the device, respectively denoted by small ($D = 30$ mm), medium ($D = 56$ mm) and large ($D = 79$ mm).

When examining the data obtained separately for each particle size, an increase in macro-scale stress with increasing paraffin content can be observed relatively unambiguously for small diameters ($d = 0.6$ mm and $d = 1.4$ mm). However, this trend is much less evident with larger diameters, which nonetheless exhibit substantially lower stress values. Furthermore, it is not possible to draw any conclusions as to the impact of cone size. Obviously, the very large dispersion of the data appear to highlight the

---

[1] https://www.cerege.fr/fr/laboratoires-et-plateformes/plateforme-matrix
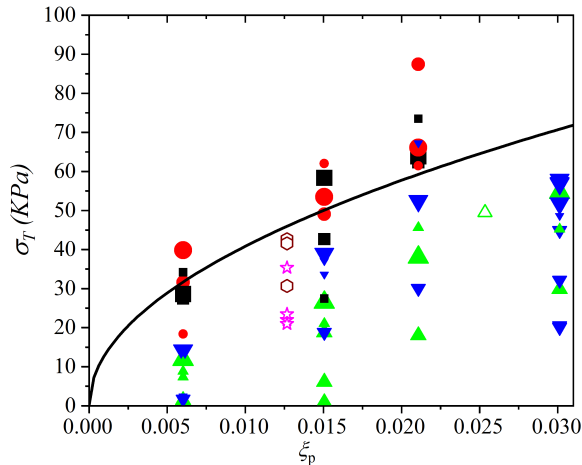
Fig. 8 Yield macro tensile stress σ_T as a function of the paraffin volume content ξ_p for different glass bead diameters, from 0.6 to 7 mm, and the three cone sizes (corresponding to the symbol sizes). Closed and open symbols represent polished and matt particles, respectively. The black curve corresponds to the theoretical prediction in Eq. 7. The different symbols stand for $d = 0.6$ mm (black squares), $d = 1.4$ mm (red circles), $d = 3$ mm (green triangles), $d = 4$ mm (blue inverse triangles), $d = 5$ mm (open brown hexagons), and $d = 7$ mm (pink stars).

inherent difficulties in the homogenization process and challenge the validity of a general definition of stress independent of the real size of the fractured surface. A related discussion will follow.

3.2 At micro-scale

The micromechanical test results are presented here first for the case of tensile loading and then for the other loading modes, i.e. shear, bending, and torsion.

3.2.1 Tensile force

Figure 9 shows the variation of the yield micro tensile force F_t with the paraffin volume fraction ξ_p for 5 different particle diameters, from 1.4 mm to 7 mm. From these results, it is observed that the yield tensile force of a bond increases with both the paraffin content and the particle size.

For each test carried with a given grain size and paraffin content, at least 10 (and sometimes up to 30) measurements were averaged to obtain a reliable mean value. Just like for the macro-tests at the sample scale, the results from the micro-tests show a very large statistical dispersion, with standard deviations on the F_t values exceeding 50 % and standard errors in the range of 20 %. Here it is also apparent that both the standard deviation and standard error increase with both particle size and paraffin content. Finally, we found no statistically significant difference in the mean tensile force value resulting from particle surface roughness (i.e. polished versus matt) with the 7 mm beads .

13
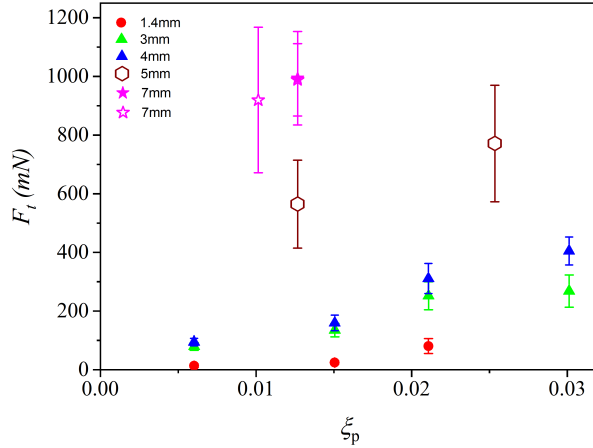
Fig. 9 Micro-tensile force F_t as a function of paraffin volume content ξ_p for different bead diameters. Closed and open markers represent polished and matt particle textures respectively, while the marker shape indicates the particle size as specified in the legend.

3.2.2 Shear, bending, and torsion loadings

This section presents further results based on other loading configurations with different particle sizes (3, 4, and 7 mm) and two paraffin mass contents (0.5 and 1 %), corresponding to around 150 additional microscopic tests. Although we have less data than for the micro-tensile tests, the critical forces measured for shear, torsion and bending show trends very similar to the former, appearing to suggest a direct proportionality between the different yield thresholds. In particular, we consider here that shear rupture is generated by a force oriented perpendicular to the axis of the solid bond, whereas bending and torsion are brought about by moments. Bending and torsion forces are therefore introduced at a distance by means of a rod; they are directed parallel and perpendicular to the axis of the paraffin bond, respectively. For dimensional consistency, the length of the lever arm is assumed equal to the diameter d of the particles and the following linear relationships are therefore considered:

$$F_s = C_s F_t \tag{2}$$

$$M_b = C_b d F_t \tag{3}$$

$$M_{to} = C_{to} d F_t \tag{4}$$

In these equations, the coefficients C_s, C_b, and C_{to} are introduced to reduce the number of independent critical thresholds for bond rupture from four to just one, here the tensile force F_t.

The approximate validity of these proportionality assumptions is illustrated in Figure 10, where the critical values of the shear force and the moment to diameter ratios in bending and torsion are plotted as a function of the yield tensile force.

14
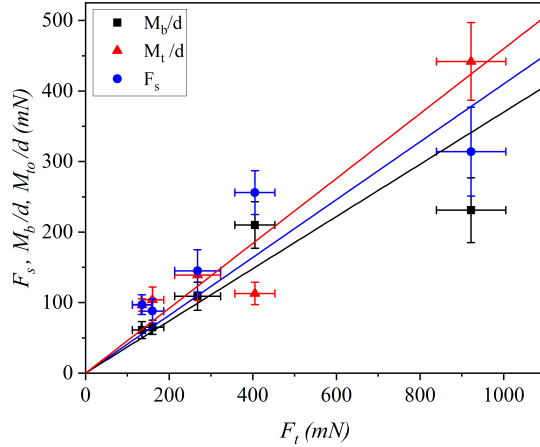
Fig. 10 Critical values of the shear force F_s and the ratios of the bending and torsion moment to the particle diameter, i.e. M_b/d and M_{to}/d, plotted as function of the corresponding yield tensile force F_t, for different particle sizes (3, 4, and 7 mm) and two paraffin mass contents (0.5 and 1 %). The solid lines stand for linear regressions using Eq. 2, Eq. 3, and Eq. 4, respectively.

The proportionality coefficients found from linear regression are $C_s = 0.41$ for shear (with $R^2 = 0.903$), $C_b = 0.37$ for bending (with $R^2 = 0.919$), and $C_{to} = 0.46$ for torsion (with $R^2 = 0.959$). It is interesting to note that they are all of the same order of magnitude, around 0.4, a value significantly higher than the $C_b \approx 0.25$ found by Delenne and co-workers in quasi-2D geometry with glued aluminium rod doublets [27]. While this assumption of proportionality between critical thresholds definitely simplifies the micromechanical model of solid bonds, we should stress that it remains a rather rough approximation that would need to be further confirmed.

It should be noted also that shearing is conducted here with no normal stress. The latter could significantly modify the behavior and failure mode, as has been studied, for example, for artificial bonds between sand grains [51].

To assess the relevance of a critical bond rupture condition associated with the moment of force in the case of bending and torsion, some additional tests were carried out. To this end, different configurations were investigated in which the length of the rod and the position of the application point of the force were modified, as shown in Figure 11 and reported in Table 3.

The critical values reported in Table 3 exhibit significant variations for force, whereas moment remains approximately the same (especially bending moment). This result indicates the relevance of the hypothesis of a critical value in moment and not in force for both bending and torsion loading on a solid bond.

15
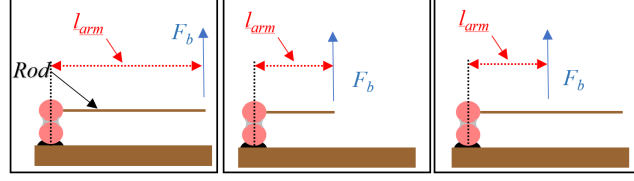
Fig. 11 Different application points of the force in the case of bending and torsion: (left) full stick edge of lever arm, (middle) half stick edge of lever arm, and (right) full stick half the lever arm.

Rod length (cm)	Lever arm (cm)	Bending Force (mN)	Bending Moment (mN.m)	Torsion Force (mN)	Torsion Moment (mN.m)
4.5	4.5	41	1.85	47	2.12
2.25	2.25	80	1.80	88	1.98
4.5	2.25	83	1.87	67	1.51

Table 3 Forces and moments obtained, for different lever arms and rod lengths in the case of bending and torsion loads, for bead diameter of 7 mm and paraffin volume content of 0.013.

3.3 Further investigation of bending and torsion by image processing from in-operando micro tests

The previous results obtained for yield forces and moments are all based on the maximal force recorded at bond rupture. However, in contrast to the tensile and shear test where the force systematically evolves linearly with spring elongation, the variations in force during bending or tension tests can be more complex and even non-monotonic as illustrated in Figure 12. If some tests show a straight linear and monotonic progression from start to final rupture, some others are not monotonic in the sense that they exhibit a linear increase of the force, then a partial release, followed by a new almost linear increase at a substantially lower rate, although a constant displacement rate of the lifting table is maintained. This unexpected non-monotonic behavior is predominantly observed for about 60 % of our torsion and bending tests.

As presented in previous Section 2.3.2, two sets of image sequences are available for more in-depth analysis of a test: one capturing the spring evolution and the other recording the positions of the flags. Using the ImageJ open-source software for basic image processing, the elongation of the spring can be precisely measured. A linear relationship is found between force and elongation, consistent with Hooke's law, and provides the value of the spring's stiffness. By post-processing the second sequence of flags images, it was possible to quantify the angle θ between the lever rod and the horizontal axis, and then examine its evolution over time.

For the minority case (around 40 % of our tests) showing a linear evolution, a pattern similar to that observed in the tensile and shear tests can be seen, as shown in Fig. 12, characterised by a gradual increase followed by a sudden drop, indicating an instantaneous break in the solid bond. The force values recovered from image processing as derived from the spring elongation are all in very good agreement with those directly recorded by the force sensor (see Fig. 12). The position flags show in

16
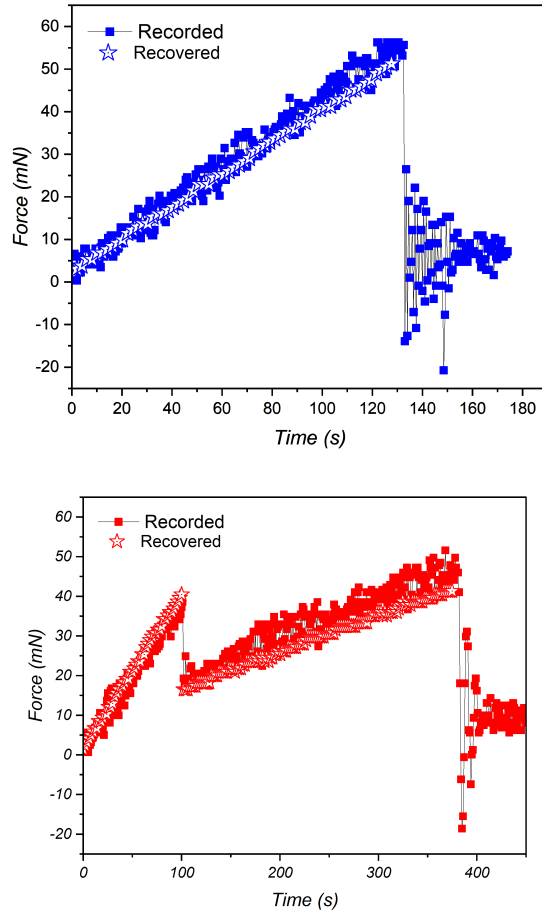
Fig. 12 Comparison between the recorded measurement and the recovered one after image post-processing giving the spring elongation for a bending test with 7 mm particles and $X_p = 0.5$ % paraffin mass content: (top) monotonic and (bottom) non-monotonic cases.

this monotonic case that the bonded couple remains immobile and stationary with relative rotation angle θ equal to zero right until bond failure, as shown in Figure 13 (blue curve). Finally, we were able to observe that the final rupture of the bond was of the adhesive type, with immediate detachment of the surface between the paraffin and the glass, as shown in Figure 14.

Then, in the same manner, we investigated the non-monotonic behavior of the force signal with an intermediate drop separating two linear segments with distinct slopes, as illustrated in the lower pane of Figure 12. We also noted that this particular signal systematically corresponded to a mixed type bond rupture, i.e., as illustrated in Fig. 14, the paraffin remains partially adhered to each of the contact surfaces on the beads, with therefore a fracture within the bond. Again, a good agreement is found between the force values recovered from spring elongation and the direct

17
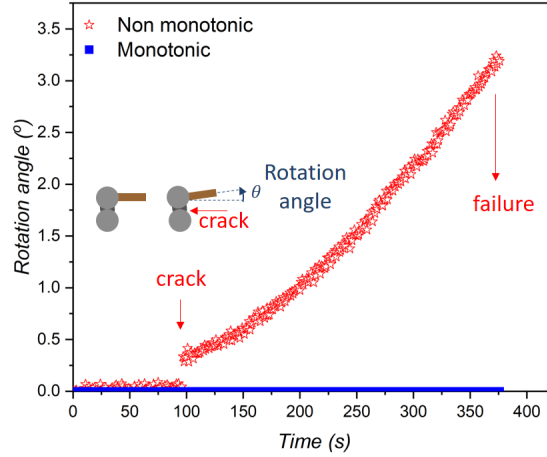
Fig. 13 Rotation of the upper glass bead in the case of non-monotonic force signal and monotonic force signal for a bending tests for 7 mm particles (Tests 1 and 2 respectively) and 0.5% paraffin content.
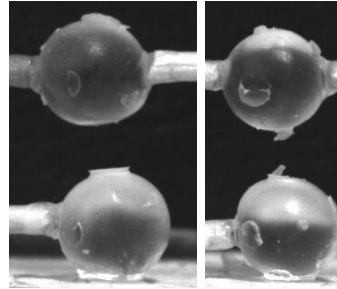
Fig. 14 Different types of rupture observed: (Left) Adhesive and (right) Mixed type.

sensor measurements, during the initial linear evolution but also with regard to the sudden drop in force. The agreement is still acceptable for the second linear increase. This means that the sudden drop in force is due to a simultaneous reduction in the elongation of the spring. There are three potential causes for this: either a bending of the rod, a loose connection of the rod to the bead (e.g. slippage relative to the clamp or displacement of the upper bead due to insufficient gluing) or rotation of the upper bead resulting in a tilt of the rod. The high stiffness of the rod in relation to the low level of force involved makes substantial deformation by bending very unlikely. The adhesive detachment of the rod can also be excluded, as nothing of this sort was observed in the sequence of images recorded during the test. The only possible reason is therefore a rotation of the lever rod leading to a reduction in the length of the spring and therefore a drop in force. This is confirmed by the image processing of the sequence recorded with the camera focused on the beads with glued flags, which gives the angle θ of the rod with respect to the horizontal. As illustrated in Fig. 13, a zero value is first found for θ, then a sudden, but limited, jump is detected at $t \approx 100$ s, followed by an almost regular increase until a value around $3 - 3.5$ ° at which the

18

paraffin bond finally breaks completely. Thus, initially, there is a normal evolution with $\theta = 0$ and the force increases linearly as validated by Fig. 12. Then, at approximately $t \approx 100$ s, a crack suddenly appears at the contact between the bottom bead and the bond, where peak stress is expected. As a consequence, there is a sudden tilt of the rod, leading to a decrease in the elongation of the spring and a consequent drop in the force signal. Next, for $t > 100$ s, the slope of the second almost linear part in Fig. 12 is found smaller due to the progressive inclination of the rod which limits the further elongation of the spring. Notably, the continuous increase in rod inclination in Fig. 13 indicates that the initiated crack is propagating even though the loading has dropped, thereby weakening the paraffin bond. In the end, this crack crosses the paraffin bond vertically to reach the upper bead, resulting in a mixed type rupture, as evidenced in the right picture of Fig. 14.

3.4 Additional insights from in-operando micro-CT scans

The micro-CT series of experiments used exclusively 7 mm matt glass beads with a paraffin mass content of 0.5 %. and included all the different types of test discussed here: tensile, shear, bending, and torsion.
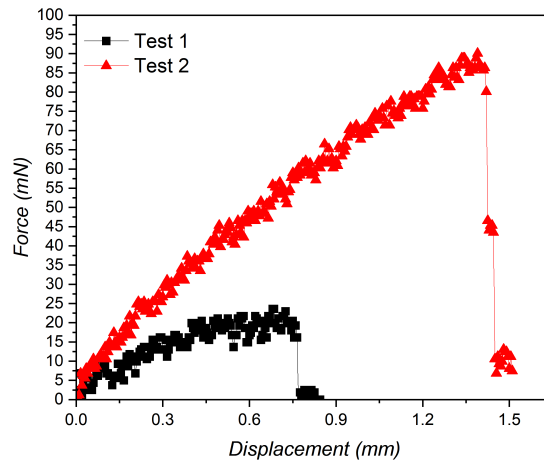
Fig. 15 Recorded torsion force measurement with loading frame displacement of the settling table during two tests for 7 mm beads with 0.5 % paraffin content in mass.

Force measurement revealed adhesive-type ruptures for tensile and shear loadings, with a linear evolution of force as a function of the displacement of the upper plate, and therefore of the elongation of the spring. In contrast, neither the torsion nor the bending tests show a comparable trend, with the observed increase in force as a function of displacement being non-linear, as illustrated for two different torsion tests with identical test parameters in Figure 15. Although the slope of the torsion test 2

remains fairly close to the value of the spring stiffness, while gradually moving away from it, this is far from being the case for test 1, which shows a very limited increase in the force applied. The micro-CT imaging provided a basis to identify and discard unreliable tests, e.g. where an insufficient fixture of the beads to the loading frame led to rigid-body rotations of the bonded pair (see Figure 16). Such unreliable tests tended to show also a non typical (highly nonlinear) force evolution.
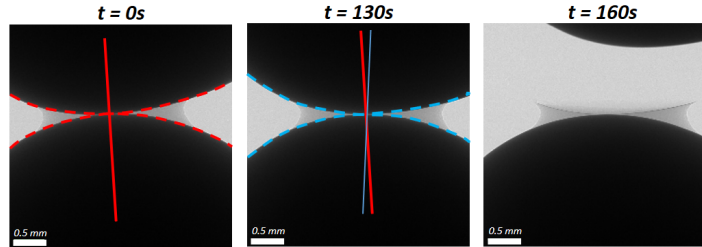
Fig. 16 Successive radiographic scans showing the entire system (both beads with bond) in rigid clockwise rotation about the vertical axis corresponding to the torsion test 1 as presented in Fig. 15. The resolution of these radiographic images is 10 μm/pixel.

Two complete 3D tomographic reconstructions of paraffin bridges after rupture were obtained. Figure 17 and Figure 18 show respectively an adhesive rupture and the only case of mixed rupture obtained. On the previous 2D radiographic scans, and even more so on these high-resolution 3D images, the absence of paraffin in the central zone is systematically observed, confirming that the particles were initially in direct contact. The images also show that the edge of the paraffin bond produces a very thin layer, which was in contact with the upper bead before the rupture and which appears to have flowed plastically (possibly due to gravity or to the displacement of the other bead) to form a sort of flattened crown.

The following conclusions can be drawn from these complementary micro-CT tests: contrary to a previous study in the literature with another type of material [5], no internal damage was observed here within paraffin as a precursor to debonding, even for a mixed-type failure, and no bond deformation was visible at this rather small scale. Moreover, the beads appeared to be systematically in direct contact.

4 Analysis and discussion

4.1 Theoretical scaling laws

4.1.1 Micro-scale tensile force

The previous experimental observations have clarified a number of basic elements for theoretical modelling. First of all, with the exception of the specific experimental configuration potentially generating a mixed bond rupture in bending and torsion, most of the time it is an adhesive failure that occurs. It is therefore a debonding force between two rigid objects that needs to be evaluated. Furthermore, as revealed by
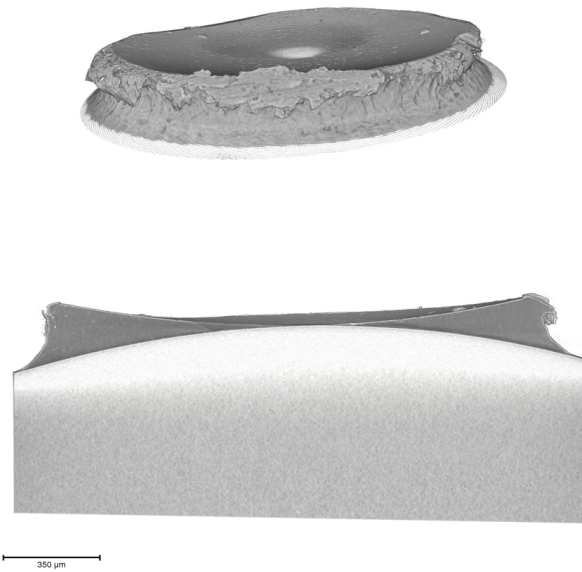
Fig. 17 3D reconstruction (top) and median radiographic scan (bottom) of an adhesive bond rupture after a shear test of 7 mm matt glass beads with 0.5 % paraffin content in mass. The resolution of both images is 2.5 μm/pixel.
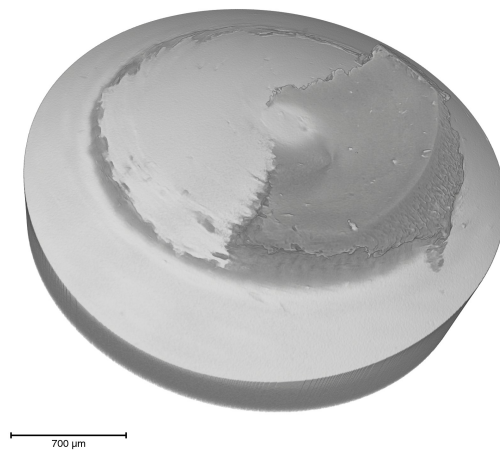
Fig. 18 3D reconstruction of a mixed bond rupture during a bending test of 7 mm matt glass beads with 0.5 % paraffin content in mass. The resolution of the image is 1.9 μm/pixel.

micro-tomography, the geometry of a bond can be represented by an almost cylindrical outer shape around two beads in real contact.

21

On this basis, we conclude that the tensile force F_t needed to debond the adhesive contact with spherical cap geometry between a rigid paraffin bridge and one of the two connected glass beads can be given by:

$$F_t = \sigma_{gp} 1.62\pi \sqrt{\frac{2}{Z}\xi_p} R^2, \tag{5}$$

where σ_{gp} is the adhesive strength at the interface between glass and paraffin and Z is the mean coordination number of the beads within the cemented sample. The theoretical basis supporting this conclusion is elaborated further in the Appendix A for the interested reader.

As shown in Figure 19, the theory provides good agreement with the experimental data when plotting F_t versus $\xi_p^{1/2} R^2$. A linear regression with 0-intercept gives indeed a proportionality coefficient equals to 0.70 ± 0.03 MPa with a R-square value of 0.978.
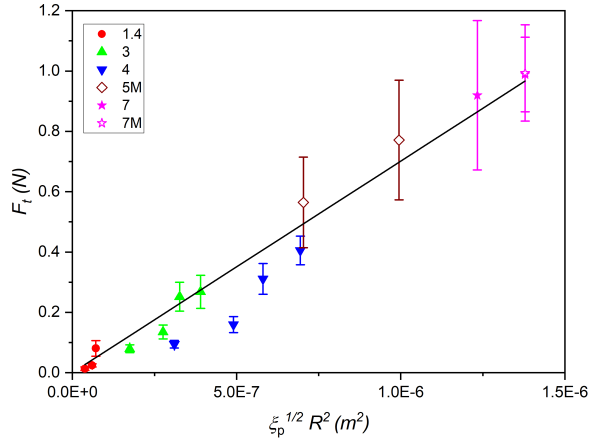
Fig. 19 Micro-tensile force F_t as a function of $\xi_p^{1/2} R^2$. The line stands for a linear regression with 0-intercept, giving a slope of 0.70 ± 0.03 MPa with a goodness of fit $R^2 = 0.978$

In order to deduce the value of σ_{gp}, we need first to estimate typical value of the mean coordination number Z in a cemented granular material which is obviously higher than in a dry granular medium since bonds can exist even if the connected grains are not perfectly in contact. An arbitrary choice of either $Z = 9$ or $Z = 8$ was previously proposed in a theoretical model of cemented granular materials [52] while, in the different but related case of unsaturated monosize grains connected by pendular water bridges, values of the coordination number tending towards 7.6 [53] and about 8 [45] have been reported. More recent studies on bio-cemented sand grains have also assumed a coordination number of 8 within the material [2, 31]. A previous work by the present authors has also suggested a value around 8 [54] for our paraffin cemented materials, consistently with a measure of 7.4 obtained for a rather similar artificial system made of beads bonded by solidified polymer bridges [32].

22

Thus, by assuming $Z = 8$ as an arbitrary but somehow relevant choice, we can finally estimate: $\sigma_{gp} = 275 \pm 12$ kPa.

Several back assessments can be made on the basis of this quantitative value. It can be first checked that this adhesive strength is consistently much smaller than the cohesive strength, or ultimate tensile strength, of paraffin for which values found in the literature (at ambient temperature and for different types of paraffin wax) indicate $\sigma_{pp} \approx 0.6$ MPa [47], $\sigma_{pp} \approx 1$ MPa [48], or $\sigma_{pp} \approx 2$ MPa [55]. Additionally, the bond strain can be estimated from Hooke's law of elasticity, with a typical Young modulus value of $E_p \sim 100 - 200$ MPa for pure paraffin wax [47, 48]. The corresponding strain reads $\epsilon = \sigma_{gp}/E_p$ and is found very small, around 10^{-3}, confirming that the bond remains almost perfectly rigid during a micro-tensile test. This result appears to validate the third assumption made for the calculation of the micro-adhesive force in Appendix A.

4.1.2 Macro-scale tensile stress

We now focus on the derivation of a micro-macro relationship of the cementation strength using the tensile test results at both the grain micro-scale and the sample macro-scale. Rumpf [43] initially formulated a homogenisation law that linearly connects the macroscopic yield stress to the inter-particle cohesion-type force. In a more recent study, Richefeu and colleagues [45] presented an expression linking the macroscopic stress σ_T to the micro-tensile force F_t, which depends on the grain radius R, the mean coordination number Z, and the mean solid volume fraction ϕ. Specifically, using Eq. 6:

$$\sigma_T = \frac{3Z\phi}{2\pi} \frac{F_t}{(2R)^2}. \tag{6}$$

Thus, by inserting Eq. 5 into Eq. 6, we obtain the following micro-macro relationship:

$$\sigma_T = 0.86\phi\sigma_{gp}\sqrt{Z}\sqrt{\xi_p}. \tag{7}$$

It is worth noting that the expression now solely depends on the paraffin volume content ξ_p and no longer includes the glass bead radius.

Figure 8 compares this theoretical relationship to the experimental data, using a coordination number $Z = 8$, a solid volume fraction ϕ of 0.61, and the value of σ_{gp} previously derived from linear regression on the micro-data. In this case, the general validity of the model remains of course unclear due to the large statistical dispersion of the data. The order of magnitude appears correct, but there may be some overestimation of the macro tensile stress.

4.2 Possible roots of intrinsic dispersion

4.2.1 At the bond scale

There are several possible reasons behind the high standard deviations. Firstly, the location from which the pair of bonded grains is extracted on the post-fracture surface of the macroscopic device may vary and be towards the centre or, on the contrary, near the periphery, with perhaps related discrepancies resulting from the method used to

prepare a macroscopic soil sample. As a result, the initial mixture of beads and liquid paraffin may not be perfectly homogeneous. There may also be slight gravity drainage of the liquid paraffin before it solidifies. Ordering effects of the grains induced by the side wall of the conical mould are also likely, especially for monosize deposits such as the ones used here. In principle, there could be a correlation between the yield force measured in the tests and the location from which the pair of grains under test is extracted, closer to the edge or deeper inside the sample.

Another source of variability could come from the intrinsic nature of the bond breakage as adhesive, cohesive, and mixed rupture are possible. In previous studies on bio-cemented soil, a wide range of bond tensile strength has been observed, regardless of the type of rupture (mixed, adhesive, or cohesive) [22, 30, 31]. In addition to high-resolution 3D tomography imaging (Fig. 17 and Fig. 18), we also identified systematically the rupture type after each micro-tensile test for 7 mm beads using a microscope with typical pictures of broken bonds shown in Figure 20. The classification is based on the presence of paraffin left on the glass beads after the bond rupture. Adhesive rupture, denoted A, is characterized by a clean surface on one of the two beads, indicating the presence of a nearly intact bond on the other bead. Cohesive rupture, denoted C, occurs within the bulk of the bond, resulting in a relatively even distribution of the paraffin deposit on the surface of both particles. Mixed rupture, denoted M, involves only a partial detachment of the bond from the beads, with only fraction of the contact surface being clean. While identifying purely adhesive rupture is straightforward, distinguishing between cohesive and mixed ruptures can become challenging and somewhat arbitrary.

All the measurements and observations carried out have shown that the type of bond rupture exhibited is influenced by several factors. Firstly, particle size plays a role. In the tensile and shear tests with particles of diameter strictly less than 5 mm (all with a polished surface finish), 100 % of the failures were indeed purely adhesive, whereas in the tests with 5 mm and 7 mm particles, a mixed type of failure was also observed. Specifically, the more detailed analysis we carried out for a series of micro-tensile tests focusing exclusively on 7 mm particles with two different surface finishes (polished and matt) shows in Figure 20 the appearance of mixed rupture and, in a single case, cohesive rupture. This study also shows a second factor influencing the type of bond rupture: the surface roughness of the beads. In effect, polished glass beads tend to undergo predominantly adhesive ruptures, whereas bond ruptures involving beads with a matt surface are mainly of the mixed type. Finally, the type of loading applied to the paraffin bond is also relevant since, as already discussed in Section 3.3, around 60% of bending or torsion tests lead to mixed-type non-adhesive ruptures, irrespective of particle size. A final effect that can be considered somewhat intuitively concerns the size of the bond. To test this possible effect, the microscope observations were used to estimate the size of each paraffin bond and to examine whether the measured bond strength increased with the cross-sectional area of the bond, as suggested by the theory (see Appendix). Surprisingly, the data revealed that the bond strength did not appear to correlate with either the bond radius or the type of rupture observed. This is clearly shown by the diagram in Figure 21, which plots the ultimate tensile force as a function of the square bond radius, irrespective of the type of rupture or the surface

finish of the beads. The blue vertical line shows the mean value of the square of the bond radius, equal to 1.12 mm^2, with the standard deviation are given by the two black lines.
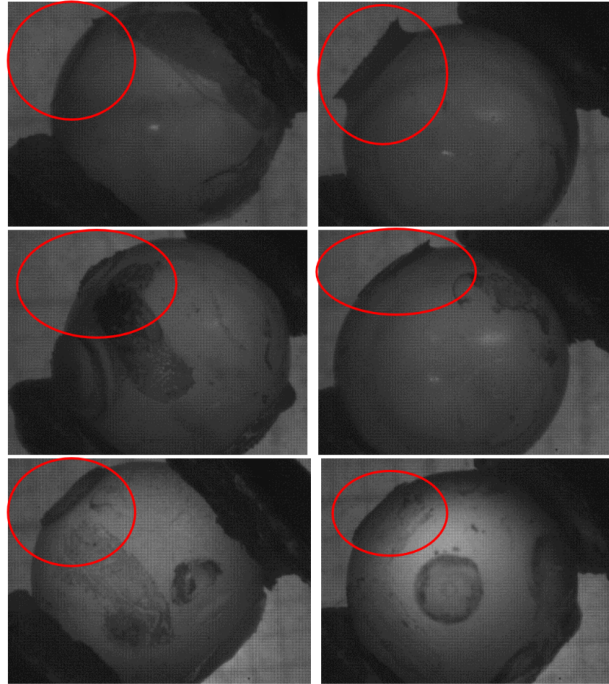
Fig. 20 Different types of ruptures for 7 mm glass beads and 0.5 % of paraffin in mass content, classified as: (top) A for adhesive, (middle) M for mixed, and (top) C for cohesive.

4.2.2 At the sample scale

On the macroscopic scale, where there is even greater dispersion than at the inter-grain scale, all the types of loading (tension, shear, bending, torsion) are simultaneously in action on the solid bonds of a cemented granular sample, particularly in the fracture zone, at the level of the minimum section of the conical moulds. It therefore seems likely that the significant deviations from the mean bond values, in terms of yield force and moment, and the associated high uncertainties on the microscopic scale are extended to the scale of the sample, where the level of uncertainty thus becomes extremely elevated. Moreover, this macroscopic dispersion can be further increased by finite size effects. As our experiments involved varying the particle size of the cemented granular samples and that of the conical devices, the number of paraffin bonds to be broken in the fracture zone can be highly variable and, in some cases, become very small, with a limited statistical mean and a potential influence of the boundary conditions as the lateral walls.
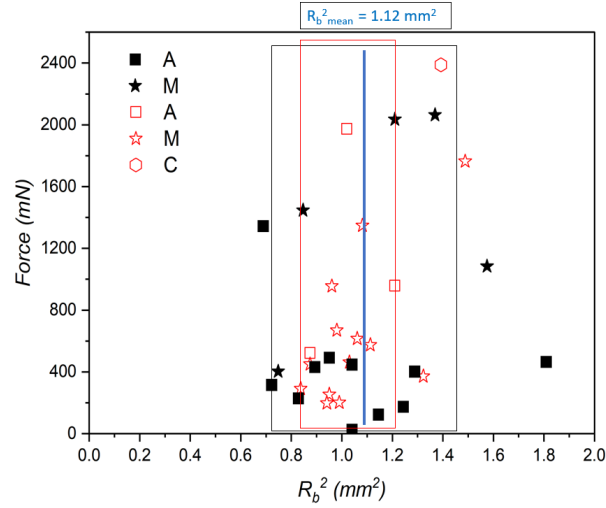
Fig. 21 Yield micro tensile force against bond radius square for 7 mm glass beads and 0.5 % of paraffin in mass content, with reference to the bond rupture type (A: adhesive, M: mixed, C: cohesive). The solid and open symbols correspond to polished and matt beads, respectively.

In addition, after the cones are separated, the exact location of the fracture within the macroscopic cemented sample shows significant variations, including 3D effects with shapes of the fracture surface that deviate from the plane and take on somewhat parabolic convex profiles, as illustrated in Figure 22. Consequently, using the minimum cross-sectional area of the device to calculate the stress at failure as suggested in Eq. 1 may lead to substantial overestimation in the cases of these non-planar shapes. To address such issues in more detail and carry out a complete study, further systematic experiments would be required, in particular to investigate any correlation between macroscopic fracture shape and structural factors such as paraffin content and particle size, especially compared to the minimum device diameter.

Fig. 22 Various shapes of rupture surface observed with the large macroscopic cone: (left) almost planar rupture for a sample of 0.6 mm beads with $X_p = 0.5$ %; (middle) roughly parabolic curved shape for a sample of 1.4 mm beads with $X_p = 0.2$ %; (right) moderately curved shape for a sample of 7 mm beads with $X_p = 0.5$ %.

4.3 Suitability of our artificial cemented soil

In view of the results achieved in the present study, this section is dedicated to a comparison of our artificial material with other models of cemented granular materials that have been considered in literature, particularly in [22, 29–31]. The choice and preparation of materials will be discussed first, followed by the phenomenology and results obtained.

The primary difference lies in the choice of binder between particles: the systems previously considered by several authors almost all feature cementation achieved by microbially induced calcite precipitation (MICP), thus replicating the main natural cementation process on site, with, in mind, various applications in geotechnics, geothermal energy, or construction material. Conversely, our choice of solidified paraffin is not directly intended to reproduce a real case but is designed for its great simplicity, allowing it to be easily modeled, either analytically, as done here, or numerically, paving the way for future benchmarks. As regards particles, we note several strategies, either using as we do glass beads as an idealized case [22, 30] or more realistic sand grains [31]. Kirsch and co-authors used particles made of the same material as the bridges, namely urea [29]. All these studies considered exclusively millimeter-sized particles. As mentioned in Section 2.1, almost all the solid paraffin is ultimately located within the bonds between particles in our material since there is no noticeable surface coating. On the contrary, MICP induces the development of calcite crystals throughout the pore space and only a fraction of them are active, in the sense that the crystals connect two grains together [31]. This also means that these bio-cemented bonds are discontinuous, consisting of several elementary bridges of calcite [31]. On the other hand, some microscopic studies have been carried out by locally bridging two particles by direct injection of bacteria into the contact zone, under conditions thus quite different from those in-situ [22, 29, 30]. Conversely, similar to Sarkis [31], we preferred here to extract bonded pairs of particles from a bulk cemented specimen, in order to retain a bond morphology representative of the specimen.

The most significant points of comparison concern the experimental results obtained, both in terms of qualitative behavior and quantitative properties. Microscopic measurements, at the scale of the cemented bond, provide the basis for positioning our artificial material in relation to the other more realistic models of cemented granular soils. First of all, the phenomenology of the micro-tests appears very generic, with a regular force increase till instantaneous bond breakage. As discussed in the previous section, the vast majority of our tests revealed adhesive ruptures of the paraffin bonds, a finding in line with that of Sarkis, who exclusively observed this type of debonding [31], whereas the distribution was more balanced between adhesive, cohesive and mixed bond ruptures in the results of Gao [30]. A very consistent observation in all studies is the considerable dispersion of these microscopic measurements. The distributions show standard deviations of at least 20 % and up to almost 70 % of the mean value [22, 31]. In this respect, it is worth noting that our estimate of the glass-paraffin adhesive strength at $\sigma_{gp} = 275 \pm 12$ kPa obtained via a linear regression based on our analytical prediction results in a much smaller error, about 4 %. Quantitatively, our tensile strength value consistently falls between the values reported in [22] and [30], which are 35 and 378 kPa, respectively. These various values

27

obtained for bonded glass beads are considerably lower than the order of magnitude around 2.8 MPa obtained by Sarkis for relatively rounded sand grains [31], probably underlining a striking effect of grain shape. As regards shear strength, it is systematically of the same order of magnitude as tensile strength, sometimes smaller as observed by Ham [22] and as we found here, and sometimes higher as is the case for the tests by Gao [30] and Sarkis [31]. Finally, from a continuous material perspective, it can be noted that our analytical expression for the macro-tensile strength in Eq. 7 is consistent with previous results in the literature showing that the sample-scale behavior of artificial cemented materials is controlled by the ratio between the porosity of the mixture and the quantity of cementing agent added [11]. At constant volume fraction ϕ as in the case here, this parameter is indeed inversely proportional to the paraffin volume fraction ξ_p.

In the end, this comparative analysis shows that, despite its atypical but very practical choice of binder, our paraffin-based artificial system behaves quite similarly to more realistic bio-cemented granular soils, with fully consistent quantitative strength values. Its ease of preparation and the simplicity of its micro-structure therefore make it well suited to parametric studies such as the one carried out in this work.

5 Conclusion

This study investigated experimentally micro- and macro-mechanical strength of a particular cemented granular materials composed of spherical glass beads bonded by solid paraffin bridges. We modified the properties of this artificial material by varying the paraffin content, the size of the beads and their surface finish, in order to test a wide range of control parameters.

We first examined several modes of loading on a microscopic scale to evaluate the bond strength, via tensile and shear forces, as well as bending and torsional moments. Despite a wide dispersion of the results (with a standard error of the order of 20 %), we observed that the yield micro tensile force increased systematically with the paraffin content and the diameter of the glass beads. Using X-ray tomography and specific experiments with subsequent image processing, we considered three different modes of rupture of the solid bond between grains: (i) adhesive rupture, where complete detachment of the bond from the surface of one of the beads occurs; (ii) cohesive rupture, where the bond itself is fractured within; and (iii) mixed rupture, which combines the characteristics of the other two modes. In general, adhesive fractures account for about 90 % of bond failures for polished particles, while mixed fractures are more frequent for matt beads. Only one case of cohesive failure has been observed for large-diameter matt beads. It should be noted that a detailed analysis did not allow us to conclusively correlate the large variations observed in micro tensile strength with either the size of the paraffin bond or its type of rupture.

To interpret our measurements in a consistent manner, we proposed a theoretical expression for the yield micro tensile force as a function of paraffin volume content, coordination number and grain diameter. Fitting the model to the data enabled us to estimate the adhesive strength at 275 kPa, with a very good accuracy of 4% despite

the wide experimental dispersion. Assuming, in addition, that there is a direct proportional relationship between the critical values of the shear force, bending moment and torsional moment and the micro tensile force, as reasonably well suggested by the experimental data with coefficients all around 0.4, made it possible to obtain a complete and fully calibrated 3D micro-mechanical model for our artificial material. By contrast, results at the sample scale are less conclusive, with even greater dispersion, making it impossible to validate the extension of the microscopic model that can be obtained directly by homogenization.

Finally, after discussing the various possible sources of variability at the micro- and macro-scale in a cemented granular material such as the present one, extensive comparisons with existing studies in the literature led to the conclusion that, although the characteristics of our artificial material made of glass beads and paraffin are significantly more distant from those of a natural bio-cemented soil, it nevertheless exhibits behavior and strength properties of the same type as the others from a mechanical point of view. Given its great simplicity and practicality of implementation, this makes it an interesting and suitable model material for benchmarking and comparative studies, particularly for calibrating or validating discrete numerical modelling approaches to cemented soil. With this in mind, work is in progress, and will be presented elsewhere, to investigate at sample scale resistance to hydro-mechanical stresses such as suction or localized upward water flow.

Declarations

Conflict of interest

The authors have no competing interests to declare that are relevant to the content of this article.

Appendix A Theory for the adhesion force of a solid bond

This section proposes a theoretical calculation for the tensile force required to separate a bridge from a sphere by considering an adhesive rupture between the two solid bodies

in contact considered both as perfectly rigid. Therefore, this approach consistently differs from the JKR type calculations, adapted to soft bond contacts [33, 34, 41], and is in line with the original analytical elements developed by Ingles [13] for a rigid bond and with more recent modelings [37, 38, 42, 56].

The calculation is conducted with the following assumptions, which are consistent with the materials and experimental conditions studied here.

- First, the mechanical load is assumed to be small enough so that the elastic deformation of the solid bridge can be neglected. This hypothesis will be verified afterwards. Note also that the deformation of the particles is still much lower when they are stiffer than the bridge, as is the case here for glass particles ($E_g \sim 65 - 70$ GPa) compared to paraffin wax ($E_p \sim 100 - 200$ MPa).

- Second, considering two perfectly rigid bodies A and B sharing a common contact surface $d\Sigma$, we will assume that the elementary force $d\vec{F}$ needed to perpendicularly debond the interface simply reads $d\vec{F} = \sigma_{AB} d\vec{\Sigma}$, where σ_{AB} is the corresponding adhesive strength between solids A and B, also sometimes called adherence [18].

- Third, the shape of a solid bridge is represented by a simplified geometry made of a cylindrical lateral envelope at the region of contact between the two bonded particles considered as spheres. Moreover, all the bridges are assumed to be strictly identical while the particles they connect are supposed to be exactly in contact. Therefore, the volume of a bridge is that of a cylinder to which it is necessary to subtract 2 spherical caps as shown on Figure A1. Considering the mode of preparation of our samples, this implies that there is a perfectly uniform distribution of the liquid paraffin within the glass beads. We will further consider that the totality of the introduced paraffin is ultimately located in the bridges, neglecting any coating on the surface out of the contacts. This appears certainly too schematic but nevertheless rather compatible with the observed visualizations (i.e. no paraffin layer is visible on the surface of the beads, even in the micro-tomographic scans).
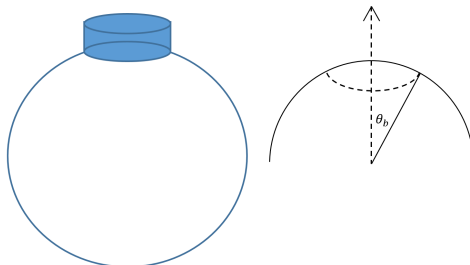
Fig. A1 Sketch of an idealized paraffin bond.

From the theoretical framework of the second hypothesis and introducing the adhesive strength σ_{gp} between glass and paraffin, the force required to detach a paraffin bridge (parameterised by the angle θ_b as shown in Fig. A1) from the surface of a glass sphere of radius R is obtained by integration over the contact surface:

$$F_t = \int_0^{\theta_b} \int_0^{2\pi} \sigma_{gp} R^2 \sin\theta \cos\theta d\theta d\varphi$$
$$= 2\pi\sigma_{gp} R^2 \left[\frac{\sin^2\theta}{2}\right] = \pi\sigma_{gp} R^2 (\sin\theta_b)^2 = \sigma_{gp}\Sigma_b \tag{A1}$$

where Σ_b is the cross section of the cylindrical bridge whose radius is $r_b = R\sin\theta_b$. One can alternatively express the F_t in a dimensionless form:

$$\overline{F_t} = \frac{F_t}{\sigma_{gp}\pi R^2} \tag{A2}$$

Note that a very similar expression than Eq. A1 is expected for a cohesive rupture, i.e. when the rupture occurs within the paraffin bridge itself. One can indeed consider that the failure surface is almost normal to the z-axis, and its area would therefore correspond approximately to Σ_b. Then σ_{gp} needs to be replaced by the intrinsic cohesive strength of paraffin, σ_{pp}, which is usually refers to as the ultimate tensile strength. For full consistency, the relation $\sigma_{gp} < \sigma_{pp}$ must be verified.

The relation between the paraffin volume content ξ_p and the bond angle θ_b is obtained relying on the third assumption, considering that liquid paraffin is exclusively located within the bonds, the latter being all identical, and that the glass spheres connected by each bond are in actual contact. The shape of a bond is consequently a cylinder minus two spherical caps and, after minor calculations, the corresponding volume V_b reads:

$$V_b = \frac{2\pi}{3} R^3 (1 - \cos\theta_b)^2 (1 + 2\cos\theta_b) \tag{A3}$$

This expression can also be written in a dimensionless form as:

$$\overline{V_b} = \frac{3V_b}{4\pi R^3} = \frac{1}{2}(1 - \cos\theta_b)^2 (1 + 2\cos\theta_b) \tag{A4}$$

In a given sample, denoting by N the number of spherical glass beads (of same radius R) with a mean coordination number Z, the total number of bonds is $\frac{Z}{2}N$. Then, we can determine in the sample the volume of paraffin V_p and glass V_g, respectively:

$$V_p = \frac{Z}{2} N V_b \tag{A5}$$

$$V_g = N \frac{4}{3}\pi R^3 \tag{A6}$$

This gives the following expression for the paraffin volume content ξ_p:

$$\xi_p = \frac{V_p}{V_g} = \frac{Z}{2}\overline{V_b} \tag{A7}$$

31

Considering $\overline{F_t}$ and $\overline{V_b}$, there is no obvious one-to-one relationship. However, the following combination can be used:

$$\frac{\overline{F_t}^2}{\overline{V_b}} = \frac{2\sin^4\theta_b}{(1-\cos\theta_b)^2(1+2\cos\theta_b)} = 2 + \frac{2\cos^2\theta_b}{1+2\cos\theta_b} \tag{A8}$$

Then, since θ_b cannot much exceed $\frac{\pi}{6}$ (i.e. limit case of a pendular bridge in a locally ordered arrangement of spheres), we can use the following approximation for $\theta_b \in \left[0, \frac{\pi}{6}\right]$:

$$\frac{\overline{F_t}^2}{\overline{V_b}} = 2.61 \pm 0.06 \tag{A9}$$

This minor approximation finally allows the following explicit semi-theoretical law to be proposed for the adhesive bond force with an accuracy of $\pm 1.2\%$:

$$F_t = \sigma_{gp} 1.62\pi\sqrt{\frac{2}{Z}}\sqrt{\xi_p}R^2 \tag{A10}$$

References

[1] Terzis, D., Laloui, L.: 3-D micro-architecture and mechanical response of soil cemented via microbial-induced calcite precipitation. Scientific Reports **8**, 1416 (2018)

[2] Dadda, A., Geindreau, C.A., Emeriault, F., Roscoat, S., Esnault Filet, A., Garandet, A.: Characterization of contact properties in biocemented sand using 3D X-ray micro-tomography. Acta Geotechnica **14**(3), 597–613 (2019)

[3] Asghari, E., Toll, D.G., Haeri, S.M.: Triaxial behaviour of a cemented gravely sand, tehran alluvium. Geotechnical Geological Engineering **21**, 1–28 (2003)

[4] Collins, B.D., Sitar, N.: Stability of steep slopes in cemented sands. Journal of Geotechnical and Geoenvironmental Engineering **137**(1), 43–51 (2011)

[5] Tengattini, A., Andò, E., Einav, I., Viggiani, G.: Micromechanically inspired investigation of cemented granular materials: part I - from X-ray micro tomography to measurable model variables. Acta Geotechnica **18**, 35–55 (2022)

[6] Marques, S.F.V., Festugato, L., Consoli, N.C.: Stiffness and strength of an artificially cemented sand cured under stress. Granular Matter **23**, 35 (2021)

[7] Ismail, M.A., Joer, H.A., Sim, W.H., Randolph, M.F.: Effect of cement type on shear behavior of cemented calcareous soil. Journal of Geotechnical and Geoenvironmental Engineering **128**(6), 520–529 (2002)

[8] Michlmayr, G., Cohen, D., Or, D.: Sources and characteristics of acoustic emissions from mechanically stressed geologic granular media - a review. Earth-Science Reviews **112**(3), 97–114 (2012)

[9] Waite, W.F., Santamarina, J.C., Cortes, D.D., Dugan, B., Espinoza, D.N., Germaine, J., Jang, J., Jung, J.W., Kneafsey, T.J., Shin, H., Soga, K., Winters, W.J., Yun, T.-S.: Physical properties of hydrate-bearing sediments. Reviews of Geophysics **47**(4), 4003 (2009)

[10] Jung, J.W., Santamarina, J.C.: Hydrate adhesive and tensile strengths. Geochemistry, Geophysics, Geosystems **12**(8) (2011)

[11] Consoli, N.C., Foppa, D., Festugato, L., Heineck, K.S.: Key parameters for strength control of artificially cemented soils. Journal of Geotechnical and Geoenvironmental Engineering **133**(2), 197–205 (2007)

[12] Powrie, W.: Soil Mechanics: Concepts and Applications, Second Edition. CRC Press, ??? (2004)

[13] Ingles, O.G.: Bonding forces in soils, Part 1: Natural soils - The physical factors responsible for cohesive strength, pp. 999–1013 (1962)

[14] Mikulčić, H., Klemeš, J.J., Vujanović, M., Urbaniec, K., Duić, N.: Reducing greenhouse gasses emissions by fostering the deployment of alternative raw materials and energy sources in the cleaner cement manufacturing process. Journal of Cleaner Production **136**, 119–132 (2016)

[15] Kou, H., Jing, H., Wu, C., Ni, P., Wang, Y., Horpibulsuk, S.: Microstructural and mechanical properties of marine clay cemented with industrial waste residue-based binder (iwrb). Acta Geotechnica **17**(5), 1859–1877 (2022)

[16] Terzis, D., Laloui, L.: A decade of progress and turning points in the understanding of bio-improved soils: A review. Geomechanics for Energy and the Environment **19**, 100116 (2019)

[17] Hu, R., Wang, X., Liu, H., Leng, H.: Scour protection of submarine pipelines using ionic soil stabilizer solidified soil. Journal of Marine Science and Engineering **10**(1) (2022)

[18] Topin, V., Delenne, J.-Y., Radjai, F., Brendel, L., Mabille, F.: Strength and failure of cemented granular matter. The European Physical Journal E **23**, 413–429 (2007)

[19] Ge, R., Ghadiri, M., Bonakdar, T., Zhou, Z., Larson, I., Hapgood, K.: Experimental study of the deformation and breakage of 3d printed agglomerates: Effects of packing density and inter-particle bond strength. Powder Technology **340**, 299–310 (2018)

[20] Chen, X., Wang, L.G., Morrissey, J.P., Ooi, J.Y.: DEM simulations of agglomerates impact breakage using Timoshenko beam bond model. Granular Matter **24**, 74 (2020)

[21] Lin, H., Suleiman, M.T., Brown, D.G., Kavazanjian, E.: Mechanical behavior of sands treated by microbially induced carbonate precipitation. Journal of Geotechnical and Geoenvironmental Engineering **142**(2), 04015066 (2016)

[22] Ham, S.-M., Martinez, A., Han, G., Kwon, T.-H.: Grain-scale tensile and shear strengths of glass beads cemented by MICP. Journal of Geotechnical and Geoenvironmental Engineering **148**(9), 04022068 (2022)

[23] Theocharis, A., Roux, J.-N., Langlois, V.: Elasticity of model weakly cemented granular materials: A numerical study. International Journal of Solids and Structures **193-194**, 13–27 (2020)

[24] Mandal, S., Nicolas, M., Pouliquen, O.: Insights into the rheology of cohesive granular media. Proceedings of the National Academy of Sciences **117**(15), 8366–8373 (2020)

[25] Jarray, A., Shi, H., Scheper, B.J., Habibi, M., Luding, S.: Cohesion-driven mixing and segregation of dry granular media. Scientific Reports **9**, 13480 (2019)

[26] Fan, X., Ten, P.H., Clarke, C., Bramley, A.S., Zhang, Z.: Direct measurement of the adhesive force between ice particles by micromanipulation. Powder Technology **131**, 105–110 (2003)

[27] Delenne, J.-Y., El Youssoufi, M.S., Cherblanc, F., Bénet, J.-C.: Mechanical behaviour and failure of cohesive granular materials. International Journal for Numerical and Analytical Methods in Geomechanics **28**(15), 1577–1594 (2004)

[28] Söderholm, K.-J.M.: Critical evaluation of adhesive test methods used in dentistry. Journal of Adhesion Science and Technology **23**(7-8), 973–990 (2009)

[29] Kirsch, R., Bröckel, U., Brendel, L., Török, J.C.: Measuring tensile, shear and torsional strength of solid bridges between particles in the millimeter regime. Granular Matter **13**(5), 517–364 (2011)

[30] Gao, K., Lin, H., Suleiman, M.T., Bick, P., Babuska, T., Li, X., Helm, J., Brown, D.G., Zouari, N.: Shear and tensile strength measurements of $CaCO_3$ cemented bonds between glass beads treated by microbially induced carbonate precipitation. Journal of Geotechnical and Geoenvironmental Engineering **149**(1), 04022117 (2023)

[31] Sarkis, M., Naillon, A., Emeriault, F., Geindreau, C.: Tensile strength measurement of the calcite bond between bio-cemented sand grains. Acta Geotechnica, 1–16 (2023)

[32] Schmeink, A., Goehring, L., Hemmerle, A.: Fracture of a model cohesive granular material. Soft Matter **13**, 1040–1047 (2017)

[33] Kendall, K.: The adhesion and surface energy of elastic solids. Journal of Physics D: Applied Physics **4**(8), 1186–1195 (1971)

[34] Chung, J.Y., Chaudhury, M.K.: Soft and hard adhesion. The Journal of Adhesion **81**(10-11), 1119–1145 (2005)

[35] Jiang, M.J., Liu, J., Sun, Y., Yin, Z.: Investigation into macroscopic and microscopic behaviors of bonded sands using distinct element method. Soils and Foundations **53**(6), 804–819 (2013)

[36] Potyondy, D.O., Cundall, P.A.: A bonded-particle model for rock. International Journal of Rock Mechanics and Mining Sciences **41**(8), 1329–1364 (2004)

[37] Ergenzinger, C., Seifried, R., Eberhard, P.: A discrete element model to describe failure of strong rock in uniaxial compression. Granular Matter **13**(4), 341–364 (2011)

[38] Brendel, L., Török, J., Kirsch, R., Bröckel, U.: A contact model for the yielding of caked granular materials. Granular Matter **13**, 777–786 (2011)

[39] Jiang, M.J., Yu, H.S., Harris, D.: Bond rolling resistance and its effect on yielding of bonded granulates by dem analyses. International Journal for Numerical and Analytical Methods in Geomechanics **30**(8), 723–761 (2006)

[40] Jiang, M.J., Yan, H.B., Zhu, H.H., Utili, S.: Modeling shear behavior and strain localization in cemented sands by two-dimensional distinct element method analyses. Computers and Geotechnics **38**(1), 14–29 (2011)

[41] Yamaguchi, Y., Biswas, S., Hatano, T., Goehring, L.: Failure processes of cemented granular materials. Phys. Rev. E **102**, 052903 (2020)

[42] Horabik, J., Jozefaciuk, G.: Structure and strength of kaolinite–soil silt aggregates: Measurements and modeling. Geoderma **382**, 114687 (2021)

[43] Rumpf, H.: The Strength of Granules and Agglomerates. New York Wiley Interscience, ??? (1962)

[44] Pierrat, P., Caram, H.S.: Tensile strength of wet granular materials. Powder Technology **91**(2), 83–93 (1997)

[45] Richefeu, V., El Youssoufi, M.S., Radjaï, F.: Shear strength properties of wet granular materials. Phys. Rev. E **73**, 051304 (2006)

[46] Brunier-Coulin, F., Cuéllar, P., Philippe, P.: Generalized Shields criterion for weakly cohesive granular materials. Phys. Rev. Fluids **5**, 034308 (2020)

35

[47] Pal, Y., Ravikumar, V.: Mechanical characterization of paraffin-based hybrid rocket fuels. Materials Today: Proceedings **16**, 939–948 (2019)

[48] DeSain, J., Brady, B., Metzler, K., Curtiss, T., Albright, T.: Tensile Tests of Paraffin Wax for Hybrid Rocket Fuel Grains, (2009)

[49] Mitarai, N., Nori, F.: Wet granular materials. Advances in Physics **55**(1-2), 1–45 (2006)

[50] Xiao, Y., Xiao, W., Wu, H., Liu, Y., Liu, H.: Fracture of interparticle MICP bonds under compression. Int J Geomech **23**, 1–12 (2023)

[51] Kasyap, S.S., Senetakis, K., Coop, M.R., Zhao, J.: Micromechanical behaviour in shearing of reproduced flat LBS grains with strong and weak artificial bonds. Acta Geotechnica **16**(5), 1355–1376 (2021)

[52] Dvorkin, J., Nur, A., Yin, H.: Effective properties of cemented granular materials. Mechanics of Materials **18**, 351–366 (1994)

[53] Gröger, T., Tüzün, U., Heyes, D.: Modelling and measuring of cohesion in wet granular materials. Powder Technology **133**, 203–215 (2003)

[54] Farhat, A., Luu, L.-H., Philippe, P., Cuéllar, P.: Multi-scale cohesion force measurements for cemented granular materials. EPJ Web Conf. **249**, 08008 (2021)

[55] Seyer, W.F., Inouye, K.: Paraffin wax: Tensile strength and density at various temperature. Industrial and Engineering Chemistry **27**, 567–570 (1935)

[56] Affes, R., Delenne, J.-Y., Monnerie, Y., Radjai, F., Topin, V.: Tensile strength and fracture of cemented granular aggregates. Eur. Phys. J. E **35**, 117 (2012)